SEDIMENTOLOGY the journal of the International Association of Sedimentologists

Sedimentology (2018) **65**, 540–560 doi: 10.1111/sed.12391

Morphodynamics and depositional signature of low-aggradation cyclic steps: New insights from a depth-resolved numerical model

AGE J. VELLINGA*†, MATTHIEU J. B. CARTIGNY*‡, JORIS T. EGGENHUISEN§ and ERNST W. M. HANSEN¶

**National Oceanography Centre, University of Southampton Waterfront Campus, European Way, Southampton, SO14 3ZH, UK (E-mail: a.j.vellinga@soton.ac.uk)*

†School of Ocean and Earth Science, National Oceanography Centre European Way, University of Southampton, Southampton, SO14 3ZH, UK

‡Departments of Earth Sciences and Geography, Durham University, South Road, Durham, DH1 3LE, UK

§Department of Earth Sciences, Utrecht University, Heidelberglaan 2, Utrecht, CS, 3584, The Netherlands

¶Complex Flow Design A.S., Havnegata 9, 7010, Trondheim, Norway

Associate Editor – Chris Fielding

ABSTRACT

Bedforms related to Froude-supercritical flow, such as cyclic steps, are increasingly frequently observed in contemporary fluvial and marine sedimentary systems. However, the number of observations of sedimentary structures formed by supercritical-flow bedforms remains limited. The low number of observations might be caused by poor constraints on criteria to recognize these associated deposits. This study provides a detailed quantification on the mechanics of a fluvial cyclic step system, and their depositional signature. A computational fluid-dynamics model is employed to acquire a depth-resolved image of a cyclic step system. New insights into the mechanics of cyclic steps shows that: (i) the hydraulic jump is, in itself, erosional; (ii) there are periods over which the flow is supercritical throughout and there is no hydraulic jump, which plays a significant role in the morphodynamic behaviour of cyclic steps; and (iii) that the depositional signature of cyclic steps varies with rate of aggradation. Previous work has shown that strongly aggradational cyclic steps, where most of the deposited sediment is not reworked, create packages of backsets, bound upstream and downstream by erosive surfaces. Here, the modelling work is focussed on less aggradational conditions and more transportational systems. The depositional signature in such systems is dominated by an amalgamation of concave-up erosional surfaces and low-angle foresets and backsets creating lenticular bodies. The difference between highly aggradational cyclic steps and low-aggradation steps can be visible in outcrop both by the amount of erosional surfaces, as well as the ratio of foreset to backset, with backsets being indicative of more aggradation.

Keywords Aggradation, backset, bedform, cyclic steps, Froude, scour, supercritical.

INTRODUCTION

Large quantities of sediment are transported by high-discharge events, such as floods or jökulhlaup (Nordin & Beverage, 1965). Such events are prone to Froude-supercritical flow, where surface waves cannot migrate upstream because the flow velocity exceeds the wave-

propagation velocity. Froude-supercritical unidirectional sediment-laden flow over an erodible sediment bed leads to the formation of bedforms, such as antidunes (Kennedy, 1969; Alexander *et al.*, 2001), and at higher Froude numbers cyclic steps (Winterwerp *et al.*, 1992; Parker, 1996; Taki & Parker, 2005; Kostic *et al.*, 2010; Cartigny *et al.*, 2014). Transitional bedforms, such as unstable antidunes and 'chutes and pools', populate the bedform stability diagram at flow-intensities between antidunes and cyclic steps (Alexander *et al.*, 2001; Cartigny *et al.*, 2014; Kostic, 2014). Supercritical-flow conditions in fluvial settings (which are open-channel flows) creating supercritical-flow bedforms have been reported in mountain streams (Kostic *et al.*, 2010), on glacial outwash planes (Lang & Winsemann, 2013), and on beaches and dredging disposal sites (Winterwerp *et al.*, 1992). Froude-supercritical conditions are reached more quickly in sediment gravity flows, such as turbidity currents and pyroclastic flows, due to the small density contrast between the flow and the ambient fluid that reduces the wave-propagation velocity. The large number of observations of Froude-supercritical flow related bedforms on the sea floor, mainly found in submarine canyons and steep delta slopes, reaffirms the prevalence of Froude-supercritical flows in marine settings (Symons *et al.*, 2016).

Developments in physical and numerical modelling of supercritical-flow bedforms (Kennedy, 1969; Jorritsma, 1973; Foley, 1977; Winterwerp *et al.*, 1992; Parker & Izumi, 2000; Alexander *et al.*, 2001; Fagherazzi & Sun, 2003; Sun & Parker, 2005; Taki & Parker, 2005; Fildani *et al.*, 2006; Kostic & Parker, 2006; Alexander, 2008; Sequeiros *et al.*, 2009; Spinewine *et al.*, 2009 Kostic *et al.*, 2010; Paull *et al.*, 2010; Cartigny *et al.*, 2011, 2014; Kostic, 2011; Balmforth & Vakil, 2012) have sparked a large number of observations of supercritical-flow bedforms in modern systems (Fildani *et al.*, 2006; Lamb *et al.*, 2008; Duarte *et al.*, 2010; Jobe *et al.*, 2011; Babonneau *et al.*, 2013; Maier *et al.*, 2013; Covault *et al.*, 2014; Hughes Clarke *et al.*, 2014; Fricke *et al.*, 2015; Tubau *et al.*, 2015; Zhong *et al.*, 2015; Normandeau *et al.*, 2016; Symons *et al.*, 2016). Despite this common and well-documented occurrence of supercritical-flow bedforms, outcrop examples of deposits indicating these flow conditions in a fluvial setting (Fielding, 2006; Duller *et al.*, 2008; Fielding *et al.*, 2009; Ghienne *et al.*, 2010; Lang & Winsemann, 2013) or in a (deltaic-) marine setting (Postma *et al.*, 2009, 2014; Ventra *et al.*, 2015; Dietrich *et al.*, 2016) are sparse. The recent flurry of recognition of supercritical bedforms in modern environments makes it implausible that sedimentary structures indicative of these bedforms should be rare in deposits formed in comparable ancient environments.

The sparsity of supercritical sedimentary structures is often attributed to poor preservation potential of supercritical-flow regime deposits, due to reworking by subcritical flows in the waning stages of high-discharge events. Froude-supercritical flows also tend to form in parts of the sedimentary system that are net-erosive on a geological timescale, such as mountainous terrains (Middleton, 1965; Foley, 1977; Yagishita & Taira, 1989; Wynn & Stow, 2002; Fielding, 2006; Duller *et al.*, 2008; Ponce & Carmona, 2011; Lang & Winsemann, 2013; Macdonald *et al.*, 2013; Cartigny *et al.*, 2014; Postma *et al.*, 2014; Ventra *et al.*, 2015). An alternative explanation for the sparse recognition of supercritical regime facies is that their depositional signature is poorly understood.

Transportational cyclic steps in open-channel flows, which are neither net-erosive nor net-depositional (Parker & Izumi, 2000), have been modelled experimentally in flume tanks (Taki & Parker, 2005; Cartigny *et al.*, 2014) and modelled numerically using depth-averaged models (Fagherazzi & Sun, 2003). Cyclic steps in subaqueous settings have been modelled in flume experiments (Spinewine *et al.*, 2009) and with depth-averaging numerical models (Fildani *et al.*, 2006; Kostic & Parker, 2006; Kostic *et al.*, 2010; Cartigny *et al.*, 2011; Kostic, 2011, 2014; Covault *et al.*, 2014, 2016). These studies have provided valuable insight into the development and mechanics of cyclic steps, by exploring how average flow velocity, sediment concentration and flow thickness vary over the length of the bedform wavelength (Fig. 1). These depth-averaged studies have also shown how the covariation of these three average properties leads to upstream migrating cyclic steps, caused by erosion beneath the accelerating supercritical flow over the lee side, and deposition beneath the subcritical flow over the stoss side. The transition between the supercritical-flow regime and the subcritical-flow regime is characterized by a hydraulic jump, where the flow abruptly expands and decelerates. Little is known about the vertical variation in flow velocity, sediment concentration, and turbulence, that occur over a cyclic step bedform, because this variation is hard to constrain with experimental measurements and averaged out in depth-averaged modelling studies. These

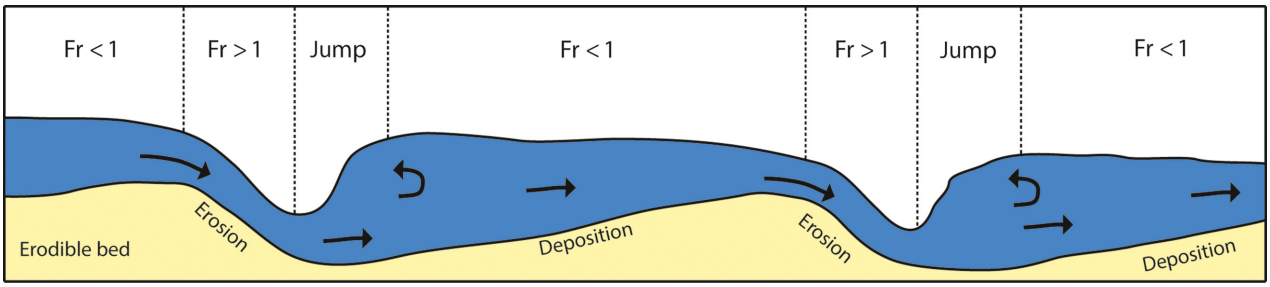

Fig. 1. A schematic drawing of a cyclic step system. The stoss side of the cyclic step is associated with a subcritical (Fr < 1) and depositional flow. The lee side of cyclic step bedform is characterized by supercritical (Fr > 1) and erosive flow. The transition between supercritical and subcritical flow is marked by a hydraulic jump.

parameters is, however, crucial to linking flow dynamics to the sedimentary architecture and facies variation over time and space. Moreover, interpreting supercritical-flow processes from outcrops and cores is strongly dependent on distinguishing small-scale facies characteristics.

The aim of this study was two-fold: (i) quantifying flow properties in a depth-resolved manner to understand the mechanics of a fluvial cyclic step system; and (ii) linking the flow dynamics of a cyclic step system to the depositional signature to predict what type of deposits are expected to be associated with cyclic steps.

METHODS

Linking large-scale bedforms and associated facies to flow dynamics in a numerical model is possible if the depositional and erosive processes are fully resolved. Ideally such a model would include a three-dimensional distribution of all fluid and grain velocities, sediment concentrations and grain sizes. Such a model would also take into account intergranular interactions between individual grains and have a two-way coupling, in which sediment is affected by fluid motion and vice versa. Direct numerical simulations (DNS) are now capable of resolving all of these processes to the individual grain scale (e.g. Cantero *et al.*, 2008; Soldati and Marchioli, 2012; Kidanemariam and Uhlmann, 2014). However, DNS is presently only viable for a small number of grains, in a relatively small spatial domain, and at low Reynolds numbers, due to the high computational power required for DNS. Because of the computational limitation on DNS, it is not a feasible method to model cyclic steps in natural flows, which have high Reynolds numbers, a large number of grains and are to be simulated over a longer timescale.

Reynolds-Averaging Navier-Stokes (RANS) models, like DNS models, employ the Navier-Stokes equations: the mass-conservation and momentum-conservation equations that describe the motion of fluids (Eqs 1.1 to 1.4 in the Appendix). Unlike DNS, RANS models do not solve the Navier-Stokes equations to the smallest spatial and temporal scale at which eddies can occur, the Kolmogorov scale, but solve time-averaged equations and use a turbulence model to approximate the small-scale turbulence. Using a RANS-approach, the computational time can be greatly reduced. Vertical variation is however maintained, in contrast to previous depth-averaging models. In this study, the RANS model FLOW-3D® (Flow Science, Santa Fe, New Mexico, USA) is used, in combination with a two-equation k-ε renormalization group (RNG) turbulence model, applying the turbulent viscosity assumption, for details see Appendix. Basani *et al.* (2014) and Ge *et al.* (2017) use the same model to simulate turbidity currents and can provide further detail.

Sediment transport models

Individual sediment transport models are used to compute bed-load transport and suspended-load transport. Grain–grain interactions are not incorporated into the suspension model, something which starts to play a significant role at sediment concentrations >9 vol.% (Bagnold, 1954). Neither does the model take into account any turbulence modification as a result of suspended sediment.

The onset of sediment movement depends on the shear stress exerted on the bed, which mobilizes the sediment, and the submerged weight of the grains, resisting mobilization. The bed shear stress is non-dimensionalized in the Shields

parameter (θ), using sediment particle scales and fluid scales (Eq. 2.1 in the Appendix). Sediment is transported if the local Shields parameter exceeds the critical Shields parameter (θcr). The critical Shields parameter is described by the Shields curve, which is approximated by an algebraic expression as formulated in Guo (2002) (Eq. 2.2). The critical Shields parameter is corrected for slope effects (Eq. 2.4) because slopes in cyclic step systems can reach up to 15 degrees.

Bed-load transport

Bed-load transport consists of the saltation and rolling of sediment along the bed, and is modelled using the empirical equation (Eq. 2.5) of Meyer-Peter & Müller (1948). The scalar quantity of bed-load transport is converted into a bed-load velocity vector, which is required to compute a directional bed-load flux (Eq. 2.6). This is done using the bed-load thickness (Eq. 2.7), as approximated by Van Rijn (1984), and by assuming that the direction of transport is the same as the flow direction of the fluid cell closest to the bed.

Suspended-load transport

Three aspects of suspended-load transport are simulated as follows: (i) sediment entrainment into suspension; (ii) sediment settling out of suspension – these two opposing processes occur simultaneously; and (iii) advection and turbulent diffusion of sediment.

A sediment-entrainment flux is expressed as a lift velocity (Eq. 2.8) which is the flux divided by the computational cell area (Mastbergen & Van Den Berg, 2003). Similarly, the settling mass-flux of sediment is calculated using Eq. 2.9 (Soulsby, 1997). The sediment velocity is calculated using the settling velocity and bulk flow velocity (Eq. 2.10). The suspended sediment concentration at a given location is computed by solving a transport equation (Eq. 2.11). The transport equation for suspended sediment incorporates both advection, using the sediment velocity from Eq. 2.10, and diffusion through turbulence.

Simulation set-up

To validate the model, the simulations are compared to an experimental study on fluvial cyclic steps (Cartigny *et al.*, 2014); this flume set-up in the EUROTANK flume laboratory is reproduced here numerically. The focus is on two experimental runs (9 and 15) which produced a stable train of cyclic steps.

The experimental flume is modelled using a meshed volume (Fig. 2) of 12·0 m by 0·15 m by 1·0 m, in the x, y and z-directions (Table 1). The width in the flow-normal y-direction has been downsized to save computational time. Boundary conditions consist of: an inflow condition, with a specified discharge, at the x = 0 m, an outflow at x = 12 m, a no-slip wall condition on the Y_{min} and Y_{max} boundaries, the sides of the flume tank, and a wall on the Z_{min} boundary, the flume tank bottom.

A smooth sediment bed of 350 μm diameter grains (medium sand) was placed on the bottom

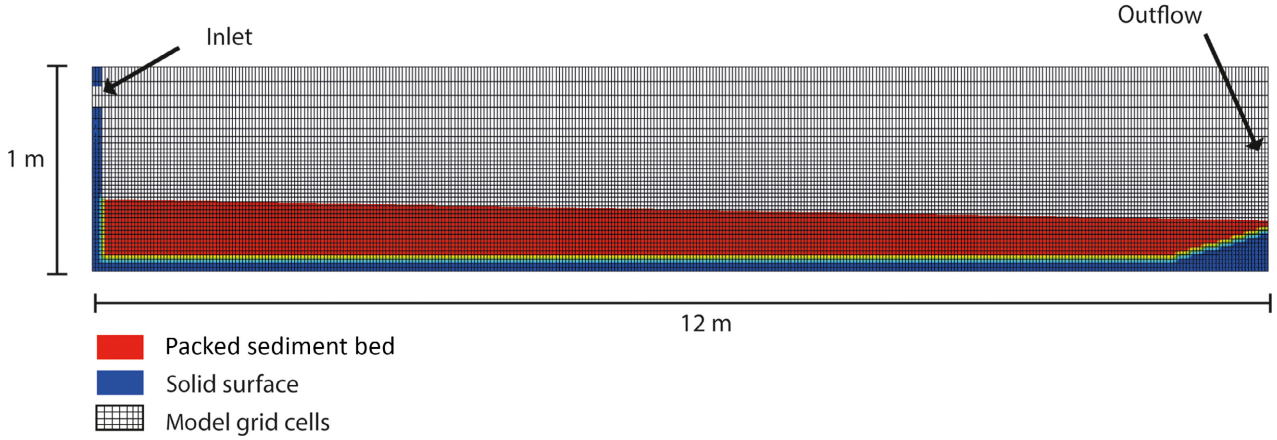

Fig. 2. The model set-up as used for the simulations, flow over the bed is from left to right. The experimental setup used in Cartigny *et al.* (2014) has a similar geometry. The packed sediment bed is indicated in red, non-erodible components are indicated in blue.

Table 1. Details on the generated mesh of the simulated domain

Direction	Size	Number of cells	Cell size (minimum – maximum)
x	12·0 m	360	3·0 cm
y	0·15 m	3	5·0 cm
z	1·0 m	38	1·8 to 8·5 cm

of the modelled flume tank with a slope of 0·5 degrees. Near the outflow boundary a non-erodible wedge is introduced to mimic a standing body of water located at the flume expansion tank, which prevents excessive erosion. The initially smooth sediment bed interacts dynamically to the flow conditions by erosion and deposition.

Numerical simulation 1 reproduced run 9 performed in the laboratory, with a specific discharge of 0·077 $m^2\ s^{-1}$ and grain size of 350 μm. Simulation 2 reproduced run 15, with a specific discharge of 0·093 $m^2\ s^{-1}$, and grain size of 350 μm (see Table 2 for details).

Validation of the model

The evolution of bed and water surface elevations displays qualitative and quantitative agreements between physical and numerical simulations (Table 3 and Fig. 3). A series of cyclic steps formed spontaneously from the initially smooth bed. Erosion and deposition in the model are validated by comparing the rates at which the cyclic steps migrate. The period of bedform migration is 109 seconds in the numerical model (numerical simulation 1), and 85 seconds in the experimental results. Cartigny *et al.* (2014) suggest that the period of migration of cyclic steps in the simulations was generally between 80 and 120 seconds, a range consistent with the numerical results.

Because flow over a cyclic step is variable by nature, a comparison is made between both the median and 90th percentile of the Froude number from the Froude number time series. Froude numbers of the numerical simulations appear to be in close correspondence with the experimental models (Fig. 3), the Froude numbers are generally <10% higher; there is, however, a 21% increase in median Froude number in simulation 1. Based on the similarity in migration period and Froude number variation, the numerical model is assumed to give a valid representation of the cyclic step process.

Table 2. Details on parameterization of the simulations

Simulation	Specific discharge ($m^2\ s^{-1}$)	Sediment concentration at inlet (vol. %)	Entrainment coefficient*	Bed-load coefficient†	Drag coefficient	Angle of repose (deg)	Packing fraction	Initial bed inclination (deg)	Turbulent length scale (m)
1	0·77	5·6	0·018	4†	1	32	0·64	0·5	0·01‡
2	0·93	5·6	0·018	4†	1	32	0·64	0·5	0·01‡

*Based on Mastbergen & Van Den Berg, 2003.
†Meyer-Peter and Muller relation, value based on Wong & Parker (2006).
‡Based on FLOW-3D release notes and manual.

Table 3. Comparison Froude numbers and migration period of experimental and numerical results

Simulation/ Experiment	Fr50	Fr90	Period migration (s)
Experimental Run 9	1·15	2·07	85
Simulation 1	1·46 (+21%)	2·25 (+9%)	109 (+30%)
Experimental Run 15	1·31	2·06	n/a
Simulation 2	1·39 (+6%)	2·21 (+7%)	118

FLOW CHARACTERISTICS

The interactions between the flow dynamics and the bedforms morphology in simulation 2 are described here in detail. The focus is on simulation 2, because the data in Table 3 show that simulation 2 is the closest match to the physical observations. Video S1 shows the flow character and the interaction with the bed, and visually complements the sections on *Flow characteristics* and *Morphodynamics*.

General character

Observation

The simulated flow creates cyclic steps that are typically 1·5 to 2·0 m in wavelength and 10 to 15 cm in amplitude, and are associated with flows 5 to 15 cm thick (for example, Fig. 4). The flow character shows that a hydraulic jump is located in or around the trough of the bedform, separating a supercritical flow on the lee side of the bedform from a subcritical flow over the stoss side (Fig. 4). In the simulations, it is observed that the hydraulic jump is present 89% of the time, which is here referred to as state 1. Flow is supercritical from crest to crest during the remaining 11% of the time (state 2). When present, the hydraulic jump is located upstream of the trough centre 50% of the time,

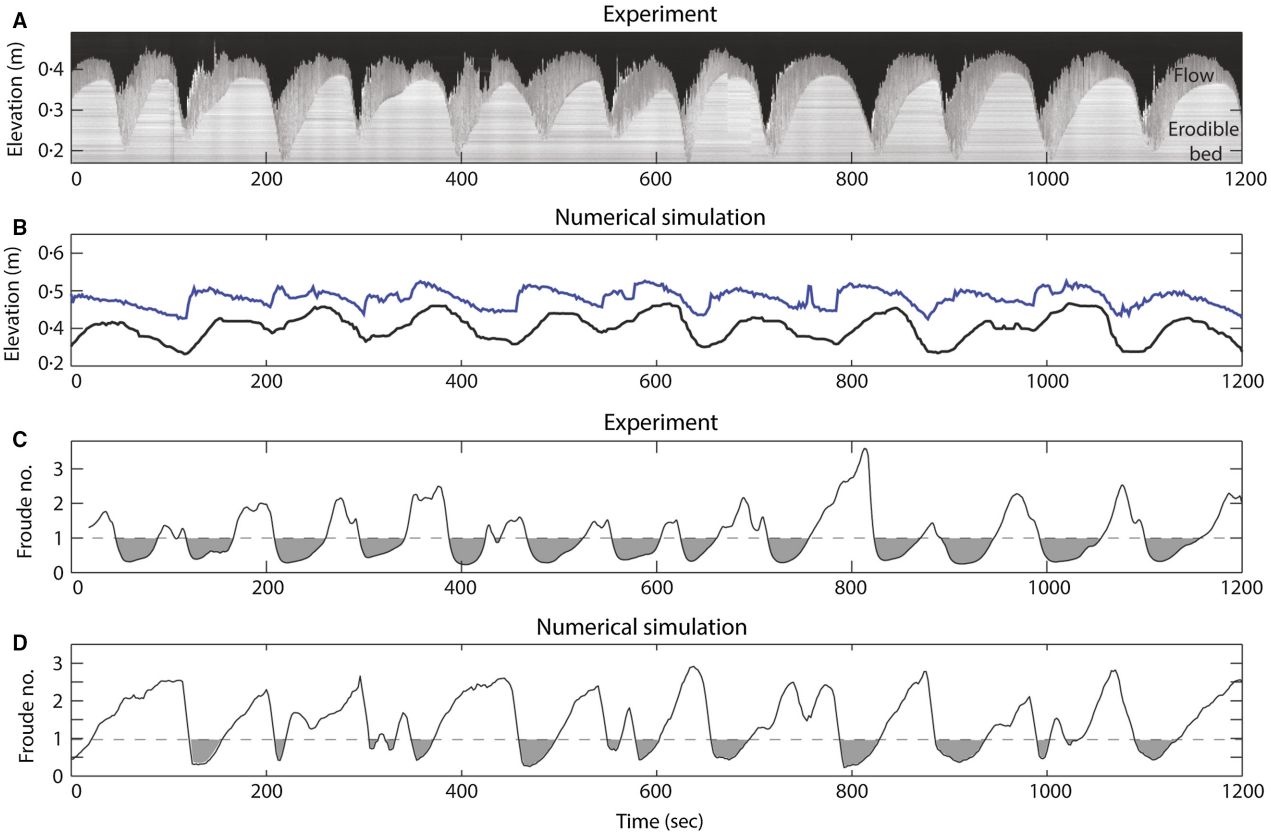

Fig. 3. Time series comparison between the experimental results of Cartigny *et al.* (2014), run 9, and numerical simulation 1 of this study. The point of reference is a stationary location in the flume; as the sediment waves migrate a time series is created. (A) The bed-surface and free-surface elevation time series in the laboratory experiment. (B) The bed-surface and free-surface elevation in the numerical simulation. (C) The Froude numbers of the experimental observations (D) The Froude numbers of the numerical simulation in this study.

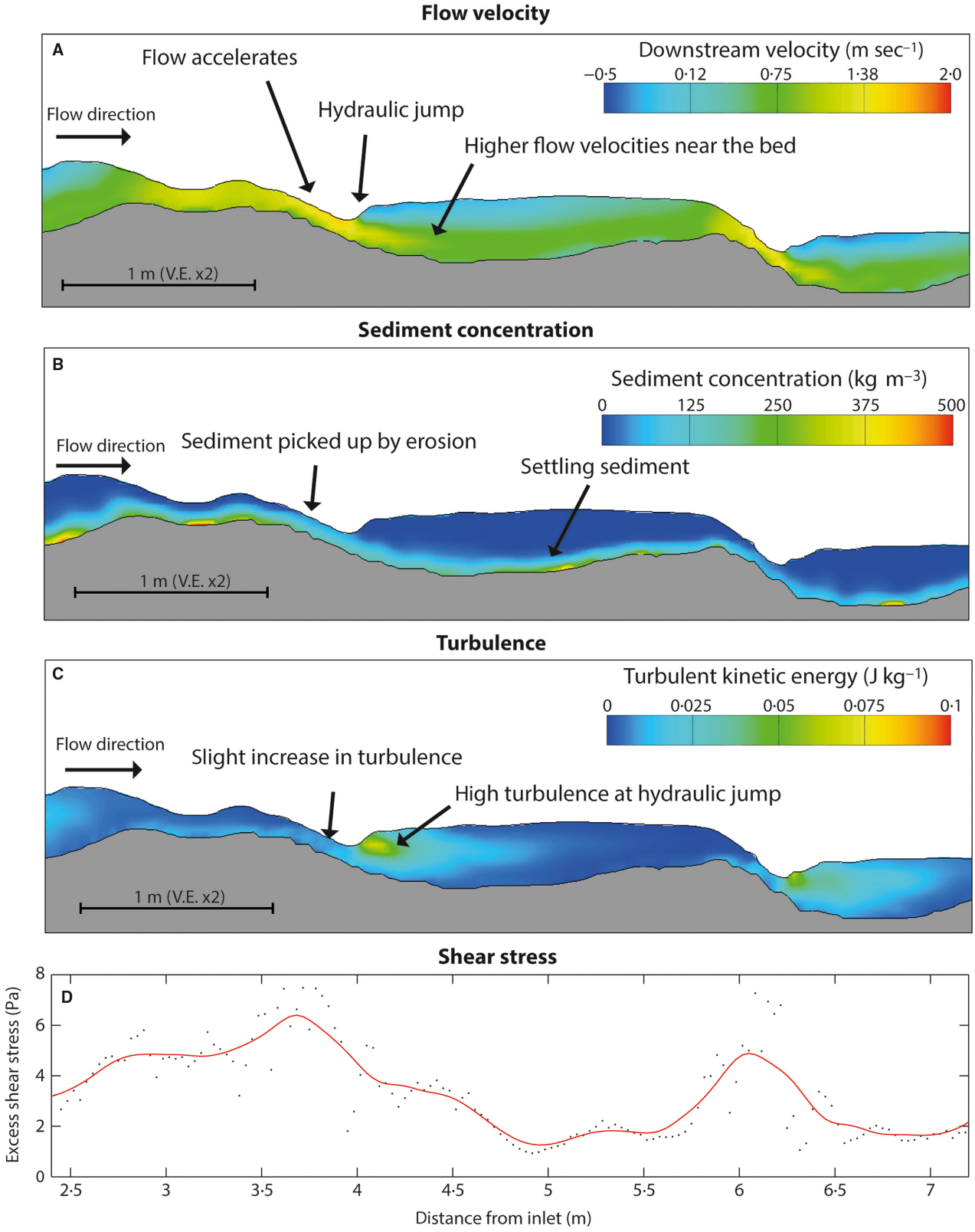

Fig. 4. Snapshots of the flow conditions in a cyclic step system, please note 2 × vertical exaggeration in the figures. (A) The downstream-velocity field over a cyclic step. (B) The sediment concentration over a cyclic step. (C) The turbulent kinetic energy over a cyclic step. (D) The excess shear stresses over a cyclic step in Pa (black dots), fitted with a 5 pt. moving average curve in red.

at the trough centre 35% of the time, and downstream of the trough centre 15% of the time. The hydraulic jump is associated with coherent flow structures, such as stationary eddies and rollers, where the water 'rolls' around and changes direction (Fig. 1). These rollers are associated with the hydraulic jump, and typically (80% of the time) located in the upper half of the flow. The remaining 20% of the time a roller forms in the lower half of the flow. The area in which rollers form is <50 cm long, starting at the initiation of the hydraulic jump, with the rollers themselves being 10 to 20 cm long and less than 10 cm high. A transition from subcritical flow to supercritical flow is present close the crest of the bedform on the stoss side of the cyclic step. The average Froude number at the crest of the bedform in the simulation was 1·22 (±0·15), based on an analysis of 29 individual cyclic steps.

Interpretation

The character of the flow over a cyclic step generally corresponds with that of conceptual models based on laboratory experiments and field observations (Fig. 1; Winterwerp *et al.*, 1992; Parker, 1996; Taki & Parker, 2005; Cartigny *et al.*, 2014). The transition from the subcritical-flow regime to supercritical-flow regime, at a Froude number of unity, is commonly presumed to be at the crest of a cyclic step (Winterwerp *et al.*, 1992; Parker, 1996; Taki & Parker, 2005; Cartigny *et al.*, 2014). The observations in simulations herein are, however, more in line with classical hydraulic work which shows that the Froude number at the crest of a curvilinear convex feature is expected to occur at Fr = 1·19 (Rouse, 1936).

Velocity field

Observation

The flow accelerates over the bedform from just after the hydraulic jump up to the next hydraulic jump. In the supercritical part of the flow velocities of 2 m s^{-1} are reached on the lee side of the bedform, and the velocity maximum is located near the free-surface. Within the region of the hydraulic jump a specific flow pattern develops; a high velocity layer located near the bed and a roller, associated with negative downstream flow velocities, is located on top of this layer (Figs 4A and 5B1). In the subcritical part of the flow the flow velocities on the stoss side range from 0·5 to 1·0 m s^{-1}.

Interpretation

The supercritical flow over the lee side of the bedform has a convex-downstream velocity profile with a large velocity gradient, creating significant shear on the sediment bed (Fig. 5B4 and 5B5). In the region of the hydraulic jump, the velocity profile is convex-downstream at the lowest section of the flow, and curved convex-upstream at the top section of the flow (Fig. 5B1); this flow structure is related to the rollers that develop in the hydraulic jump. The velocity profile downstream of the hydraulic jump (Fig. 5B2 and 5B3) is not typical for open-channel flow as it inherits the unusual velocity profile caused by the hydraulic jump.

Sediment concentration

Observation

The average sediment concentration in the flow is 5·6% by volume. A clear increase in sediment concentration over the supercritical lee side of the cyclic steps is not observed (Figs 4B and 5C). At the region of the hydraulic jump, there is a clear difference in sediment concentration between the fast-flowing near-bed layer, with concentrations between 5% and 10%, and the upper part of the flow, where sediment concentrations within the roller are less than 1% (Fig. 5C1 and 5C2). In the subcritical part of the flow the near-bed sediment concentrations range from 5 to 10% by volume. Sediment concentrations decrease towards the free surface, where they reach near-zero values (Fig. 4B).

Interpretation

The lack of increase in sediment concentration over the lee side of the cyclic steps is counter-intuitive, as one might think that entrainment of sediment into the flow increases the sediment concentration. However, the sediment discharge is the product of the sediment concentration and flow velocity. And while depth-average sediment concentration only increases from 7 to 9%, the sediment discharge doubles over the lee side (Fig. 6F). This doubling shows that an increasing velocity forms the dominant control on the sediment discharge and explains the counter-intuitive sediment concentration trend. There is in an increase in stratification in the subcritical part of the flow, the sediment settles, causing higher sediment concentrations near the bed (Figs 4B, 5C2 and 5C3).

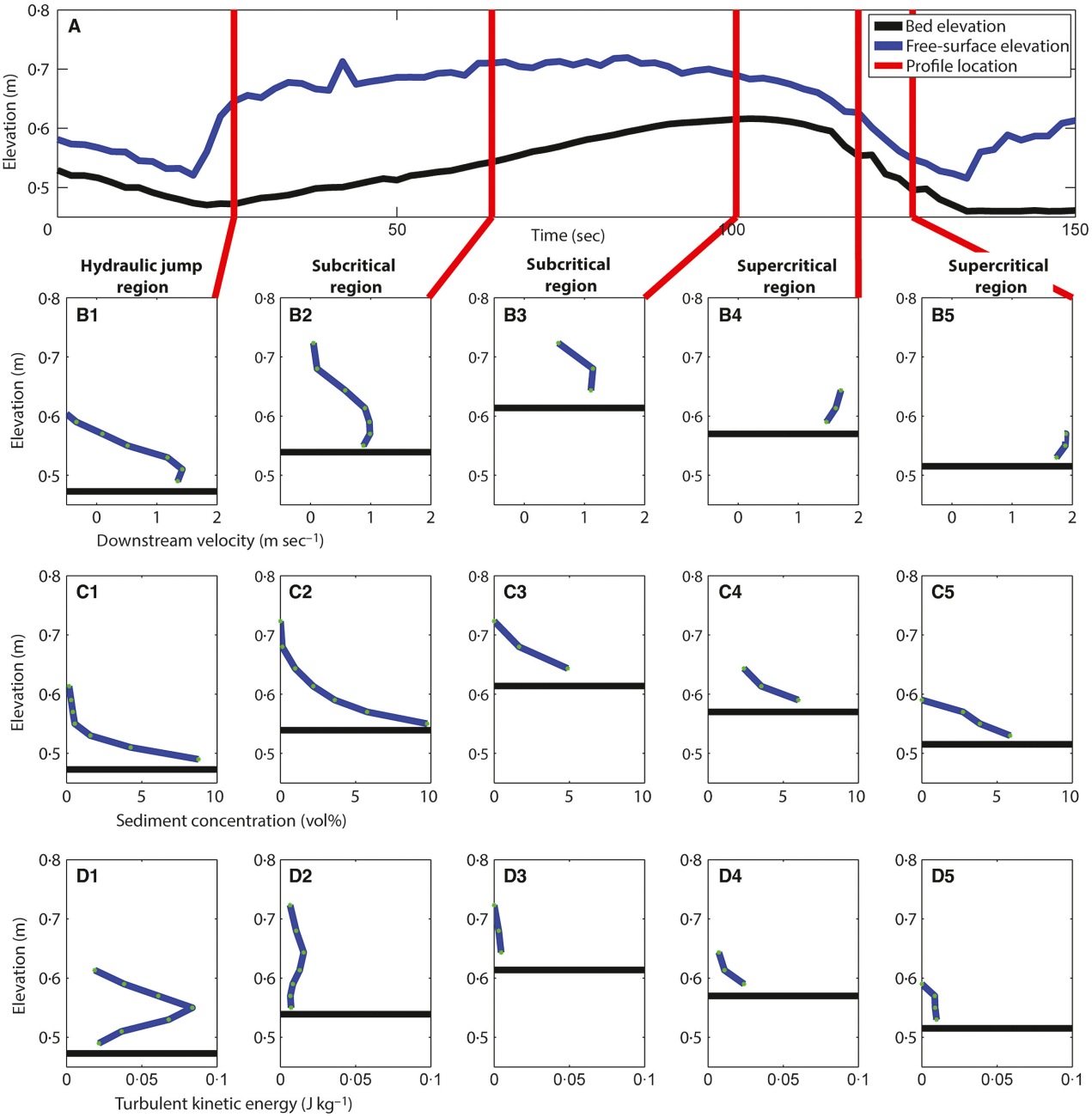

Fig. 5. Profiles through the flow, one cyclic step wavelength (A), based on time series data, showing downstream velocity (B), sediment concentration in (C) and turbulent kinetic energy (D).

Turbulence

Observation

Turbulent kinetic energy (TKE), the mean kinetic energy per unit-mass associated with turbulent eddies, is of the order of 0·01 to 0·03 J kg^{-1} in the supercritical part of the flow, with peak values near the bed where shear is highest (Fig. 5D4 and 5D5). These TKE levels are equivalent to 8 to 14 cm s^{-1} of turbulent velocity fluctuations assuming isotropic turbulence. TKE is three to ten times higher (0·1 J kg^{-1}) in the region of the hydraulic jump (Figs 4C and 5D1). The subcritical region has the lowest turbulent kinetic energy, generally less than 0·01 J kg^{-1}.

Interpretation

Turbulence is generated in flow regions where shear within the flow is high (i.e. the velocity

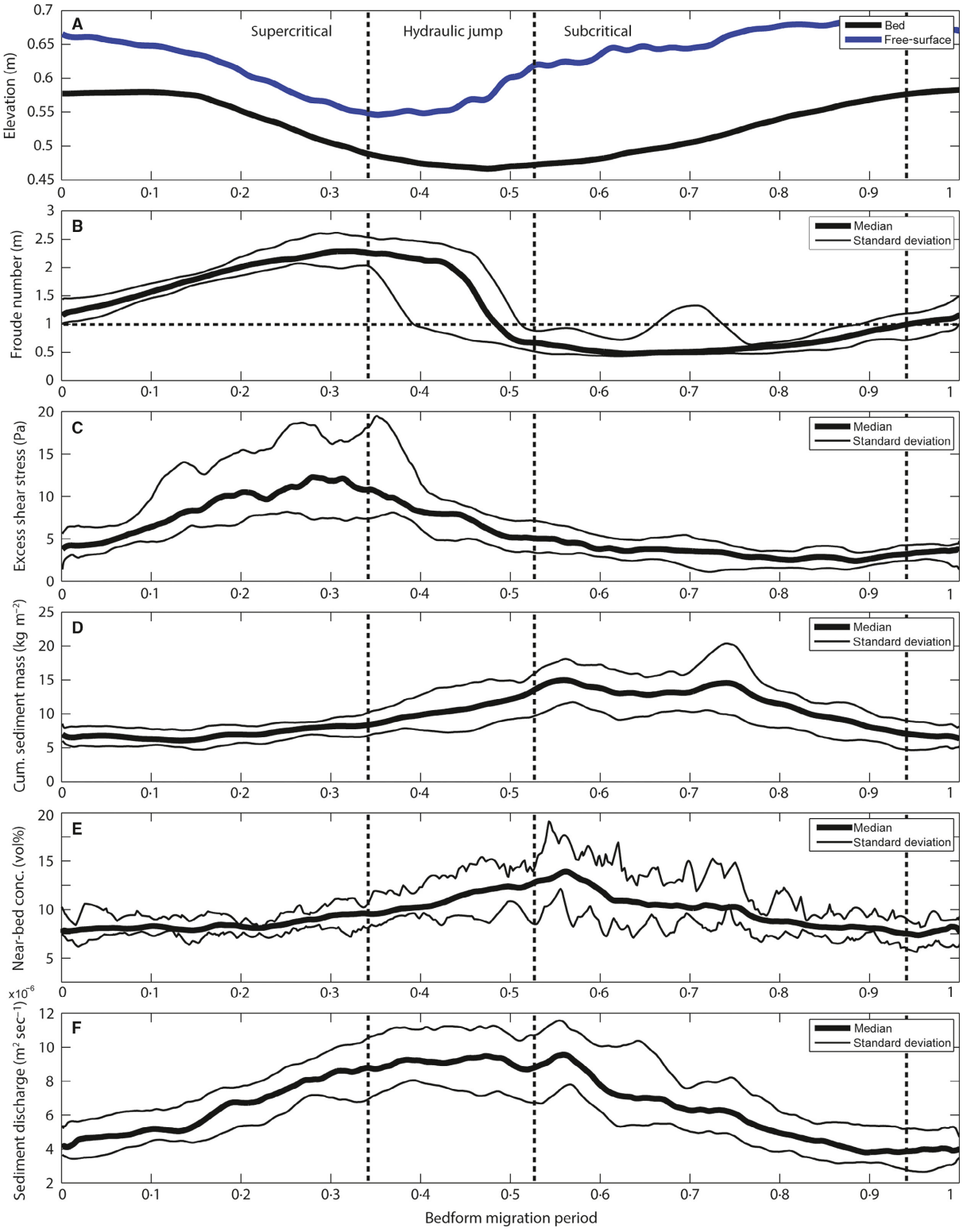

Fig. 6. Six time series plots of different physical properties over a cyclic step during one migration period. The properties are median or average properties based on 12 individual cyclic steps. One full migration period is displayed on the *x*-axis (0 to 1). The graphs display: (A) average bed elevation and free-surface elevation; (B) median Froude number; (C) median shear stress; (D) median depth-integrated (cumulative) sediment mass; (E) median near-bed sediment concentration, where near-bed is defined as the two computational cells closest to the bed; (F) median downstream sediment flux (sediment discharge).

gradient), such as the case at a hydraulic jump. Turbulence is the mechanism through which sediment is suspended and dispersed in the flow. Hence, in regions of high turbulence sediment is not prone to settle, despite having relatively high sediment concentrations. The combination of high turbulent energy, inhibiting settling, and a relatively high shear on the bed at the hydraulic jump is a likely cause for entrainment to outpace settling, causing the hydraulic jump region itself to be erosive.

MORPHODYNAMICS

Relating the flow dynamics to bed-surface evolution is crucial to understand how cyclic steps maintain their morphodynamic equilibrium. Described here are two states observed in a cyclic step system between which the system alternates (Fig. 7). State 1 (89% of the time): there is a hydraulic jump present in the trough of the bedform, the flow is supercritical at the lee side of the cyclic step, and subcritical at the stoss side of the cyclic step. State 2 (11% of the time): the flow is supercritical over the whole bedform and a hydraulic jump is absent, the flow over the stoss side of the bedform decelerates and thickens, but not enough to form a hydraulic jump. In state 2, the flow is still erosive over the lee side of the bedform, and depositional over the stoss side. The topographic difference between the trough of the bedform and the crest is lower in state 2 than in state 1. Videos S1 and S2 help to visualize and understand the morphodynamics more clearly.

Flow state 1

Observation

Supercritical flow is limited to the crest and lee side of the cyclic step in flow state 1. The excess shear stress, the shear stress that exceeds critical shear stress for movement on the bed (here 0·25 Pa), increases from 5 Pa at the crest of the bedform, to 13 Pa just before the hydraulic jump (Fig. 6C). An excess shear stress larger than 0 does not mean that there is overall erosion, but simply that there is some sediment entrainment. It is the local balance between the sediment-entrainment flux, which increases with shear stress, and the settling flux, which determines whether there is net erosion or net deposition.

The start of the hydraulic jump is typically located at the downstream end of the lee side and is associated with the transition from the lee side to the stoss side. The hydraulic jump is mildly erosive, illustrated by its location on the lee side (Fig. 6A). The excess shear stress decreases gradually from about 13 Pa to 5 Pa within the region of a hydraulic jump (Figs 4D and 6C).

After the flow has decelerated at the hydraulic jump, the flow slowly thins and accelerates again, while depositing sediment at the stoss side. The shear stress in the subcritical part of the flow is 4 to 5 Pa (Fig. 6C). Both the increase in bed height and the decrease in sediment discharge (Fig. 6A and F) illustrate that the Froude-subcritical region is depositional.

In state 1, more sediment is deposited nearer the trough of the bedform than at its crest, causing the topography to decrease (Fig. 7D and E). As the topography decreases, the hydraulic jump is washed out and disappears.

Interpretation

In state 1, the continuous acceleration of the supercritical flow over the lee side of the bedform leads to increased bed shear stress. Upstream of the crest of the bedform (0·95 to 1·0 on Fig. 6), shear stresses on the bed are low enough to allow the settling of sediment to outpace entrainment of sediment. Downstream of the crest of the bedform shear stress continuously increases, resulting in the sediment-entrainment flux exceeding the settling flux, making the flow erosive, as indicated by an increase in sediment discharge (Fig. 6F). The morphological effect of the supercritical flow is a curve at the crest of the bedform towards a linear lee side of the bedform.

At the hydraulic jump, erosion is caused by high shear stresses and increased turbulence. High shear stress is explained by relatively high velocities near the bed in the hydraulic jump region (Figs 4A and 5A1). Increased turbulence in this region, caused by coherent flow structures, allows sediment to remain in suspension and inhibits settling. The amount of sediment stored in the water column increases over the hydraulic jump region (Fig. 6D). As a result, the morphological effect of the hydraulic jump is a transition from a steep and strongly erosive lee side, through a concave trough, and to a depositional upstream-dipping stoss side.

In the subcritical flow region, the sediment-entrainment flux is smaller than that of sediment settling flux, as low bed shear stresses limit the entrainment. The low turbulence levels in the subcritical region cause the sediment picked up on the lee side to settle. Sediment

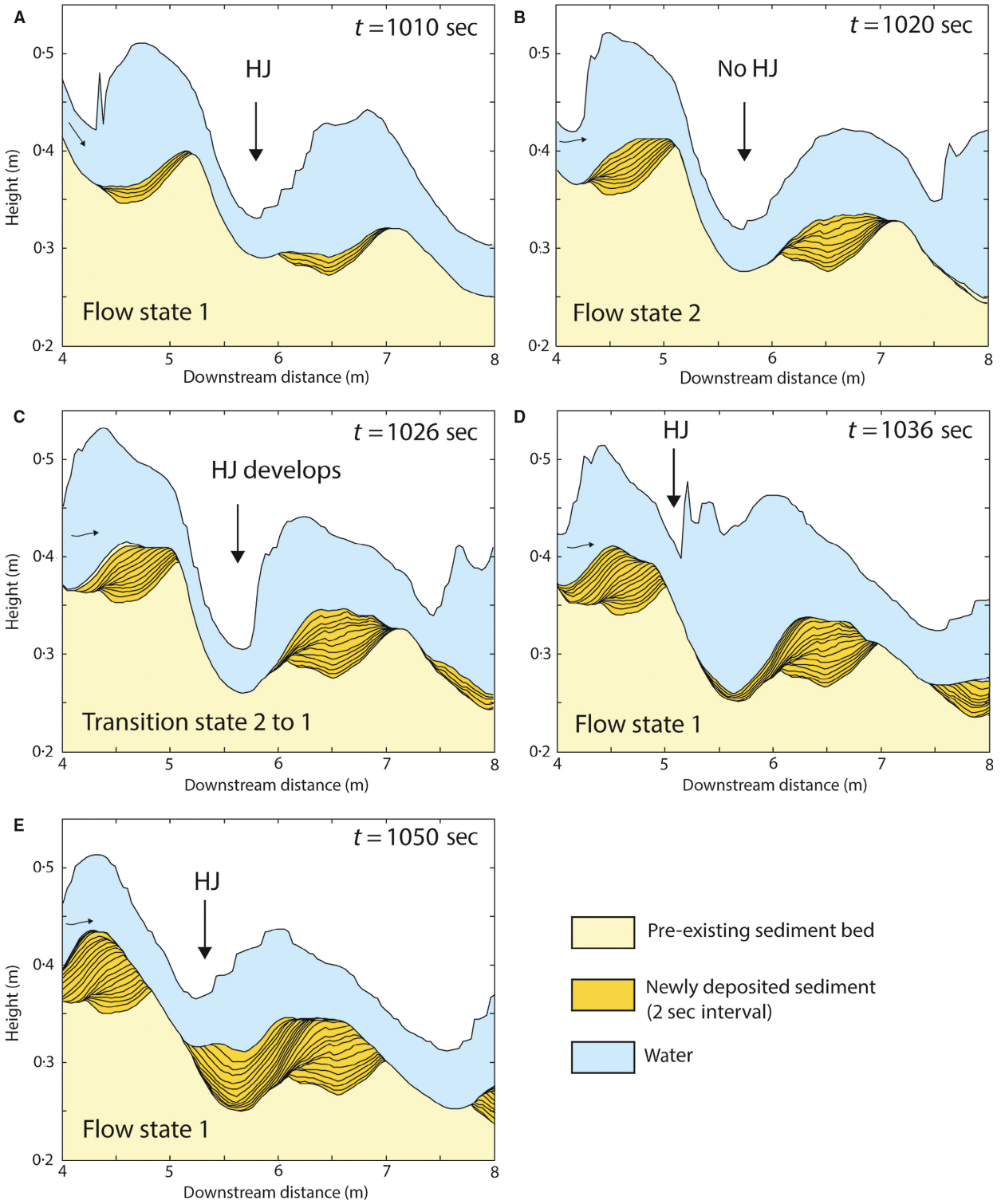

Fig. 7. Five panels showing the flow behaviour during different stages of the cyclic step system, also shown are the associated newly formed deposits. The lines in the newly formed deposit are two-second timelines.

grains collect at the base of the flow before settling (Fig. 6E), thereby causing flow stratification as a result of limited mixing. The morphological response to this depositional subcritical flow region is an increase in bed elevation over the stoss side, with more sediment being deposited

close to the trough than near the crest, effectively decreasing the topography between crest and trough, setting up the system to change to flow state 2.

Flow state 2

Observation

In state 2, supercritical flow prevails over the entire bedform. Even though the flow thickens over the stoss side of the bedform towards the crest, the flow remains supercritical. The thicker supercritical flow on the stoss side is still depositional with excess shear stresses ranging from 5 to 7 Pa.

More sediment is deposited at the crest than in the trough in flow state 2, thereby increasing the topography (Fig. 7B). Such increased topography caused by deepening of the trough and deposition on the crest triggers the formation of a new hydraulic jump (Fig. 7B and C).

Interpretation

In state 2, the lee side of the cyclic step remains erosive. Notwithstanding the supercritical-flow conditions, the stoss side of the bedform is still depositional as the settling flux exceeds the sediment-entrainment flux.

The morphological behaviour in state 2 is not unlike that of antidunes, because more sediment is deposited near the crest than at the trough the topography of the bedform to increases. When comparing the flow parameters with the bedform geometry through the empirical equations of Kennedy (1960) and Alexander *et al.* (2001), it is clear that the bedforms are, however, not antidunes. An increase in topography in flow state 2 sets up the system to create a new hydraulic jump and return to flow state 1. The hydraulic jump forms at the crest of the bedforms and migrates towards the trough. This alteration between two flow states, with depositional patterns that inherently require an alteration from one state to another, is also described in a carbonate ramp setting which is interpreted to have backset beds formed by cyclic steps (Slootman *et al.*, 2016). The cycle alternating between flow states 1 and 2 appears to be an autogenous interplay between bed topography and the flow, and is inherent to the depositional pattern of the two flow states.

DEPOSITIONAL SIGNATURE

Sedimentary structures can be indicative of palaeoflow conditions and therefore provide an aid to reconstruct the palaeoenvironment. Hence, it is important to understand the formative processes of bedforms and their associated sedimentary structures. Here, the modelling results are used to directly link the flow process to the depositional product. The cyclic step simulations provide flow conditions at the moment of deposition for each subgridded sediment parcel at every time step, and hence the model not only builds up a series of sedimentary structures, but is also able to link the individual parts of these sedimentary structures with their flow conditions during deposition.

Discussed herein is the development of the depositional architecture (Fig. 8A to E) and the parameters that control the sedimentary facies. Video S2 visually complements the subsection regarding *Architecture*. The discussed parameters are as follows: (i) the sediment concentration near the bed (Fig. 8F); (ii) the flow regime, represented by Froude number (Fig. 8G); and (iii) the bed shear stress (Fig. 8H), an important factor in how erosive or depositional the flow is, and responsible for grain-size trends.

Architecture

The architecture of the deposit associated with a cyclic step system is dependent on the rate of aggradation. In an aggradational system, the architecture consists of upstream-dipping laminations (<10°), called backsets, which form on the depositional stoss side of the bedform (Fig. 9A) (Kostic & Parker, 2006; Spinewine *et al.*, 2009; Yokokawa *et al.*, 2009; Lang & Winsemann, 2013). The backsets onlap onto a composite erosional surface at their upstream side, which forms the lower set-boundary. The backsets are truncated at their downstream side by a similar erosive surface, forming the upper set-boundary. The simulations in this study are not aggradational but transportational; this is reflected by a different depositional architecture (Fig. 9B). The resulting depositional architecture is an amalgamation of concave-up erosion surfaces and small portions of preserved low-angle backsets and foresets creating mostly concave-up lenticular bodies (Fig. 9B).

The development of the architecture of transportational cyclic steps in Fig. 9B is seen in Fig. 8A to E. A deep trough that formed during washout of the hydraulic jump is filled by sediment (Fig. 8B). The sediment laps onto the erosion surface as a foreset with a downstream transition into a backset (<5°). This creates a

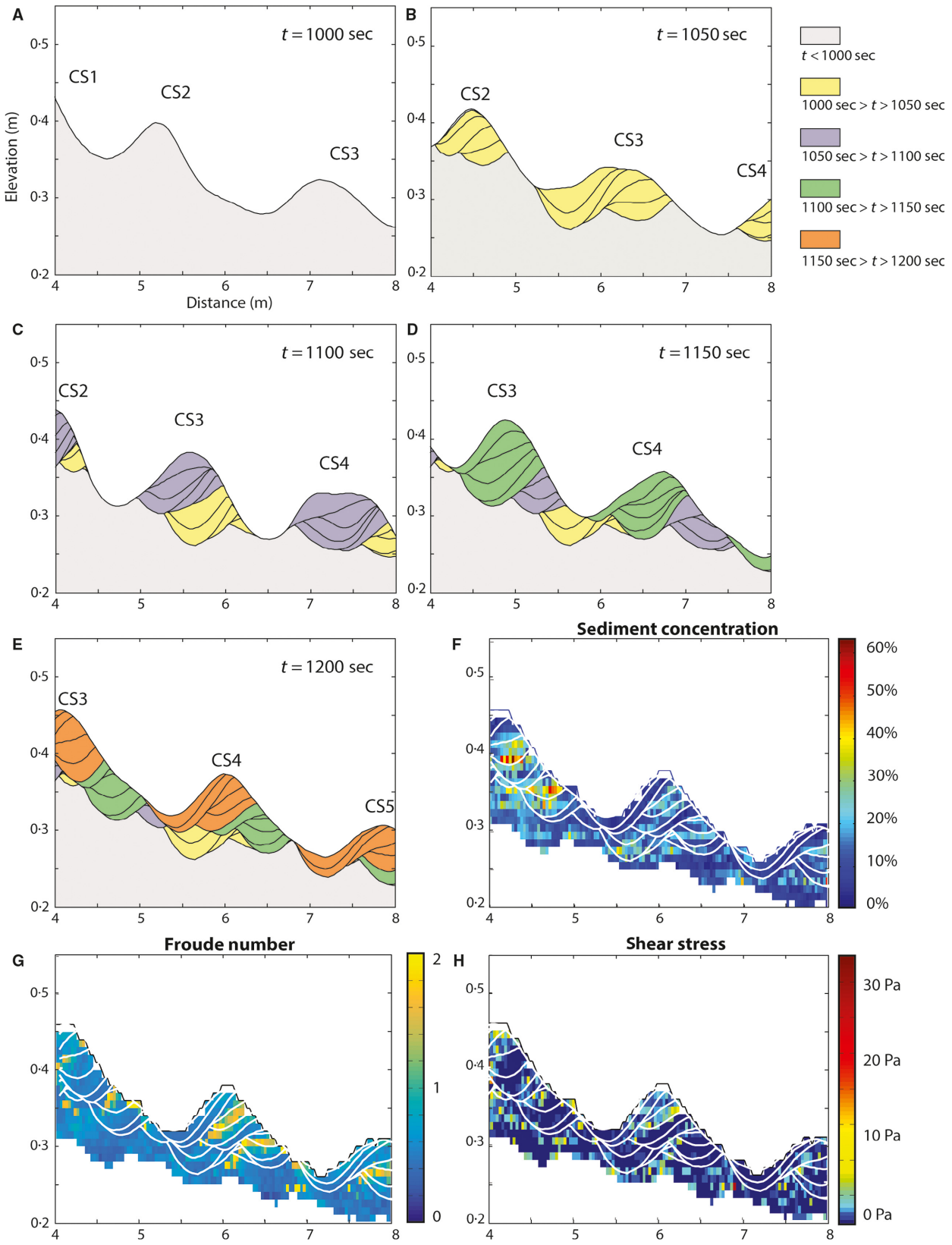

Fig. 8. Panels (A) to (E) show the development of the depositional architecture of a transportational cyclic step system at 50-second time intervals, with 10 second 10 time-lines within these intervals. Panels (F) to (H) display near-bed sediment concentration, Froude number, and shear stress at the moment a sediment parcel got deposited.

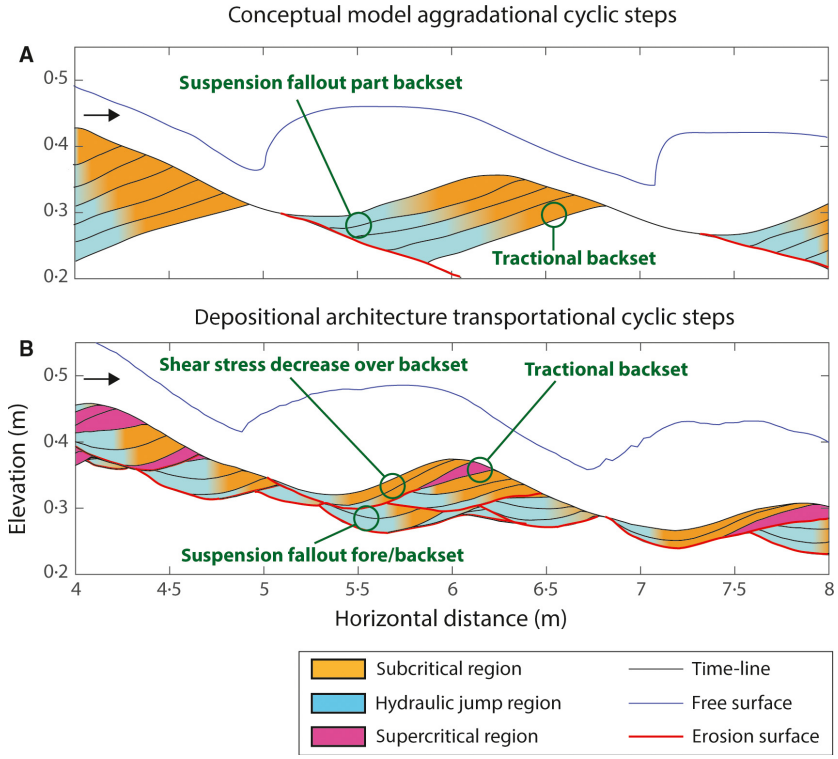

Fig. 9. Depositional architectures of aggradational cyclic steps (A) and more transportational cyclic steps (B). The figure also shows the inferred flow regime at which the deposits were formed. Please note that the black lines are time-lines, and not necessarily laminations due to grain-size breaks.

concave-up deposit (Fig. 8B). A large portion of the deposited backsets is eroded by the upslope migration of the successive bedform (Fig. 8A to E). The deposits shown in Fig. 8B are mostly reworked in Fig. 8C, and only the deepest trough infill near the initial onlap is preserved. These deepest trough deposits form below the hydraulic jump. If the flow is supercritical throughout (state 2), steeper backsets and more tabular backsets are formed (Fig. 8D). These steeper, tabular backsets (<10°) are less likely to be preserved because they form near the crest, which is more prone to erosion. During the transition from state 2 (supercritical throughout), to state 1 (with hydraulic jump), erosion can occur on the stoss side, leading to upstream truncation of the laminations.

Sediment concentration

The sediment concentration at the moment of deposition over a cyclic step (Fig. 8F) is generally lower than 9% by volume. Deposits that form under subcritical flow form at lower near-bed sediment concentration (*ca* 5%) than the deposits formed under supercritical flow (*ca* 8%) (Fig. 8F). The flow is generally dilute (<9 vol.%) in all regions (Fig. 5C), implying that turbulence is the dominant grain support mechanism (Bagnold, 1954).

Flow regime

Even though a cyclic step is characterized by supercritical flow over the lee side, the deposits are predominantly formed in the subcritical-flow regime (Fig. 8G). Traces of bedforms associated with the subcritical-flow regime, such as current ripples, superimposed on the larger scale bedform, could therefore be formed as a consequence. Bedform stability diagrams indicate that flow over proximal backset deposits are within the ripple regime (Van den Berg & Van Gelder, 1993). Ripples have been associated with subcritical flow after a hydraulic jump in the distal part of hydraulic jump bars (Macdonald *et al.*, 2013). Given the high settling rate following the hydraulic jump such current ripples could initially be climbing. Ripples are, however, not simulated in the numerical model due to a lack of resolution. Deposition during supercritical-flow

conditions (state 2) also results in a backset (Fig. 8G). Backsets deposited during supercritical flow onlap further downstream than those formed at subcritical conditions and are steeper.

Shear stress

Cyclic step deposits show alternation in bed shear stress over time and space (Fig. 8H). Variability in shear stress over time would lead to a variation in grain size from one backset stratum to another, creating lamination, and thereby delineating individual backset strata. In general, shear stresses at the moment of deposition decrease from trough to crest (Fig. 9B). Deposits that form directly after the rapid erosion have the lowest shear stresses as a roller forms below the main flow (20% of the time), see Fig. 9B. In the absence of a hydraulic jump, shear stresses over the stoss side are relatively high, and there is increased traction on the bed where the deposits form (Fig 9B).

The simulations in this study show a decrease in shear stress over the stoss side of the bedform (Fig. 6C). A downstream fining over individual backsets can be caused by a decrease of flow competence to carry sediment (i.e. a decrease in shear stress), or can be due to a decrease in flow capacity to carry sediment. Submarine cyclic steps are suggested to be downstream fining, but not due a decrease in shear stress, because shear stress is suggested to increase over the stoss side (Postma & Cartigny, 2014). The downstream fining, as described by Postma & Cartigny (2014), would be caused by a decrease in the capacity of the flow to carry sediment. Both the capacity and competence arguments can be used to explain downstream fining (Hiscott, 1994). Open-channel flows and turbidity currents both can create cyclic steps, but are different in many ways, in velocity profile and concentration profile to start with, and in shear stress pattern as a consequence. Both a decrease in flow capacity and a decrease in flow competence can produce downstream fining, and it is possible that the two mechanisms play different roles in marine and fluvial systems, but ultimately lead to a similar result; a downstream fining.

CONSEQUENCES FOR OUTCROP STUDIES

Recognition of cyclic step deposits in outcrop is strongly dependent on the preservation potential of the deposits, and whether cyclic step systems are aggradational or transportational (Fig. 9). Deposits associated with strongly aggradational cyclic steps have a different depositional signature than deposits resulting from transportational cyclic steps.

A highly aggradational cyclic step system in outcrop may resemble the deposit such as seen in Fig. 9A, which represents an idealized deposit. There is a clear sequence of backsets that are separated by set boundaries at the upstream side and at the downstream side. Downstream fining within sets results in a normal grading in the vertical due to progressively upstream emplacement of the backsets. Such depositional signatures of aggradational cyclic step systems are, however, uncommon in fluvial outcrops, where clear sequences of continuously stacked backsets are absent due to a lack of accommodation space. In marine and deltaic settings, accommodation space is more readily available, and the character described above is observed in outcrop (Ventra *et al.*, 2015; Dietrich *et al.*, 2016) and in shallow seismic imagery (Migeon *et al.*, 2000, 2001, 2006; Normark *et al.*, 2002; Fildani *et al.*, 2006; Flood *et al.*, 2009; Gilbert & Crookshanks, 2009; Heinio & Davies, 2009; Zhong *et al.*, 2015).

Cyclic steps that are transportational have a different depositional signature (Fig. 9B) than aggradational ones. The overall depositional signature is an amalgamation of lenticular bodies bound by erosion surfaces. Similar to the backsets formed in an aggradational setting, backsets formed in a transportational setting are downstream fining. The deposited backsets are reworked for a large part; on the downstream side by upstream migrating erosion, and on the upstream side when the hydraulic jump gets washed out. At the washout stage of a hydraulic jump the trough migrates upstream rapidly and erodes underlying sediments creating a deep new trough. Sediments deposited in this trough create a concave-up lens, with the best preservation potential of the flow, as the trough cuts deep into the substrate, out of reach of subsequent erosion. The concave-up bodies formed at low shear stress conditions may be associated with suspension fallout due to a decrease in flow capacity. Backsets that form when the flow is supercritical throughout (state 2) are steepest, as they enhance the existing topography. These backsets also form under relatively high shear stress where there is traction on the bed, grain sizes in these backsets are likely to be larger

than average as fines will not be able to settle under these conditions (decrease in flow competence). These transportational cyclic step deposits resemble those observed in small-scale laboratory experiments (Yokokawa *et al.*, 2009).

When comparing the simulated depositional signature to that in the geological record, it is important to appreciate differences of scale. Cyclic step facies have been interpreted in outcrops of deltaic settings (Dietrich *et al.*, 2016) and glacial flood outbursts (Duller *et al.*, 2008; Lang & Winsemann, 2013). In these settings, concave-up troughs are filled with diffusely laminated backsets. The troughs are typically several metres long and the backsets within them vary in steepness between 5° and 20° (Duller *et al.*, 2008; Lang & Winsemann, 2013; Dietrich *et al.*, 2016). The numerical results show a very similar architecture, but on a smaller scale. Both in this study and in outcrop, distinct concave-up troughs are filled by diffusely laminated foresets and backsets that dip 5° to 15° (Fig. 9B); Erosion surfaces in the simulations dip in the order of 5° to 15° (Fig. 9B); their abundance and the size of the preserved backsets are dependent on the rate of aggradation. The faint stratification described in Duller *et al.* (2008) and Lang & Winsemann (2013) is probably due to a change in shear stress on the bed related to the stages in which the flow is supercritical throughout. Dietrich *et al.* (2016) show a series of upstream-dipping backsets that are indicative of more aggradational cyclic steps, as these backsets are not cross-cut by an erosive surface but rather a more continuous stack of backsets such as seen in Fig. 9A. More aggradation yields fewer erosional surfaces as well as more preservation of backsets relative to foresets.

CONCLUSIONS

The depth-resolved numerical model allows a unique insight into the mechanics of a cyclic step system, and the modelling results can be used to link the mechanics to the depositional signature. The simulated cyclic steps generally adhere to existing conceptual models, with Froude-supercritical flow over the lee side and Froude-subcritical flow over the stoss side of the bedform. The hydraulic jump affects a large flow region and is often itself erosive. A hydraulic jump is not always present, and occasionally the flow is only supercritical, but still deposits at the stoss side. In absence of a hydraulic jump, the bedform amplitude is enhanced and leads to the formation of a new hydraulic jump.

The depositional signature of a cyclic step system is dependent on the rate of aggradation. In the case of a high aggradation rate, a package of backsets, bound upstream and downstream by erosion surfaces, can be found. In more transportational systems, the deposited backsets will be reworked to a large degree. The depositional signature of cyclic steps is dominated by an amalgamation of concave-up erosional surfaces and low-angle foresets and backsets creating lenticular bodies. This depositional signature is determined to a large extent by the transient nature of the hydraulic jump as it migrates upstream and downstream with respect to the trough location, and is occasionally washed out entirely. Similar geometries are visible over a range of scales in outcrop studies. Variation in shear stress at the moment of deposition, probably related to the presence or absence of a hydraulic jump, results in more pronounced backsets of a distinct grain size.

ACKNOWLEDGEMENTS

ExxonMobil is acknowledged for funding this research. Riccardo Basani and Romain Rouzairol are thanked for their help and advice during the modelling phase of this study. Arnoud Slootman is acknowledged for fruitful discussions on the subject of cyclic step morphodynamics. We acknowledge support from NERC grant (NE/P009190/1) "New field-scale calibration for turbidity current impact modelling" which is part of the Environmental Risks to Infrastructure Innovation Programme (ERIIP). Aaron Fricke, Pierre Dietrich, Svetlana Kostic and Jorg Lang are thanked for their valuable reviews that have improved the manuscript significantly. Data used in this study is available from the author on request.

REFERENCES

Alexander, J. (2008) Bedforms in Froude-supercritical flow, in marine and river dune dynamics proceedings, p. 1–5

Alexander, J., **Bridge, J. S.**, **Cheela, R. J.** and **Leclair, S .F.** (2001) Bedforms and associated sedimentary structures formed undersupercritical waterfows over aggrading sand beds. *Sedimentology*, **48**, 133–152.

Babonneau, N., **Delacourt, C.**, **Cancourt, R.**, **Sisavath, E.**, **Bachelery, P.**, **Mazuel, A.**, **Jorry, S. J.**, **Deschamps, A.**, **Ammann, J.** and **Villeneuve, N.** (2013) Direct sediment transfer from land to deep-sea: insights into shallow

multibeam bathymetry at La Reunion Island. *Mar. Geol.*, **346**, 47–57.

Bagnold, R. A. (1954) Experiments on a gravity-free dispersion of large solid spheres in a Newtonian fluid under shear. *Proc. Roy. Soc. London Ser. Math.Phys. Sci*, **225**, 49–63.

Balmforth, N. J. and **Vakil, A.** (2012) Cyclic steps and roll waves in shallow water flow over an erodible bed. *J. Fluid Mech.*, **695**, 35–62.

Basani, R., **Janocko, M.**, **Cartigny, M. J. B.**, **Hansen, W. M.** and **Eggenhuisen, J. T.** (2014) MassFLOW-3D TM as a simulation tool for turbidity currents : some preliminary results. In: *Depositional Systems to Sedimentary Successions on the Norwegian Continental Margin* (Eds A. W. Martiunus, A. Ravenas, J. A. Howell, R. J. Steel and J. P. Wonham) *Special Publication 46 of the IAS*, **46**, 587–608.

Cantero, M. I., **Balachandar, S.**, **García, M. H.** and **Bock, D.** (2008) Turbulent structures in planar gravity currents and their influence on the flow dynamics. *J. Geophys. Res. Oceans*, **113**, 1–22.

Cartigny, M. J. B., **Postma, G.**, **van den Berg, J. H.** and **Mastbergen, D. R.** (2011) A comparative study of sediment waves and cyclic steps based on geometries, internal structures and numerical modeling. *Mar. Geol.*, **280**, 40–56.

Cartigny, M. J. B., **Ventra, D.**, **Postma, G.** and **van Den Berg, J. H.** (2014) Morphodynamics and sedimentary structures of bedforms under supercritical-flow conditions: new insights from flume experiments. *Sedimentology*, **61**, 712–748.

Covault, J. A., **Kostic, S.**, **Paull, C. K.**, **Ryan, H. F.** and **Fildani, A.** (2014) Submarine channel initiation, filling and maintenance from sea-floor geomorphology and morphodynamic modelling of cyclic steps. *Sedimentology*, **61**, 1–24.

Covault, J. A., **Kostic, S.**, **Paull, C. K.**, **Sylvester, Z.** and **Fildani, A.** (2016) Cyclic steps and related supercritical bedforms: building blocks of deep-water depositional systems, western North America. *Mar. Geol.* https://doi.org/10.1016/j.margeo.2016.12.009

Dietrich, P., **Ghienne, J.-F.**, **Normandeau, A.** and **Lajeunesse, P.** (2016) Upslope-Migrating Bedforms In A Proglacial Sandur Delta: cyclic Steps From River-Derived Underflows? *J. Sed. Res*, **86**, 113–123.

Duarte, J. C., **Terrinha, P.**, **Rosas, F. M.**, **Valadares, V.**, **Pinheiro, L. M.**, **Matias, L.**, **Magalhães, V.** and **Roque, C.** (2010) Crescent-shaped morphotectonic features in the Gulf of Cadiz (offshore SW Iberia). *Mar. Geol.*, **271**, 236–249.

Duller, R. A., **Mountney, N. P.**, **Russell, A. J.** and **Cassidy, N. C.** (2008) Architectural analysis of a volcaniclastic jökulhlaup deposit, southern Iceland: sedimentary evidence for supercritical flow. *Sedimentology*, **55**, 939–964.

Fagherazzi, S. and **Sun, T.** (2003) Numerical simulations of transportational cyclic steps. *Comput. Geosci.*, **29**, 1143–1154.

Fielding, C. R. (2006) Upper flow regime sheets, lenses and scour fills: extending the range of architectural elements for fluvial sediment bodies. *Sed. Geol.*, **190**, 227–240.

Fielding, C. R., **Allen, J. P.**, **Alexander, J.** and **Gibling, M. R.** (2009) Facies model for fluvial systems in the seasonal tropics and subtropics. *Geology*, **37**, 623–626.

Fildani, A., **Normark, W. R.**, **Kostic, S.** and **Parker, G.** (2006) Channel formation by flow stripping: large-scale scour features along the Monterey East Channel and their relation to sediment waves. *Sedimentology*, **53**, 1265–1287.

Flood, R. D., **Hiscott, R. N.** and **Aksu, A. E.** (2009) Morphology and evolution of an anastomosed channel network where saline underflow enters the Black Sea. *Sedimentology*, **56**, 807–839.

Foley, M. G. (1977) a Quantitative Hydrodynamic Indicator I. *J. Sed. Petrol*, **47**, 738–746.

Fricke, A. T., **Sheets, B. A.**, **Nittrouer, C. A.**, **Allison, M. A.** and **Ogston, A. S.** (2015) An examination of Froude-supercritical flows and cyclic steps on a subaqueous lacustrine delta, Lake Chelan, Washington, U.S.A. *J. Sed. Res*, **85**, 754–767.

Ge, Z., **Nemec, W.**, **Gawthorpe, R. L.** and **Hansen, E. W. M.** (2017) Response of unconfined turbidity current to normal-fault topography. *Sedimentology*, **64**, 1–28.

Ghienne, J.-F., **Girard, F.**, **Moreau, J.** and **Rubino, J.-L.** (2010) Late Ordovician climbing-dune cross-stratification: a signature of outburst floods in proglacial outwash environments? *Sedimentology*, **57**, 1175–1198.

Gilbert, R. and **Crookshanks, S.** (2009) Sediment waves in a modern high-energy glacilacustrine environment. *Sedimentology*, **56**, 645–659.

Guo, J. (2002) Hunter Rouse and Shields diagram.: advances in Hydraulic and Water. *Engineering*, **2**, 1096–1098.

Heinio, P. and **Davies, R. J.** (2009) Trails of depressions and sediment waves along submarine channels on the continental margin of Espirito Santo Basin, Brazil. *Geol. Soc. Am. Bull.*, **121**, 698–711.

Hiscott, R. N. (1994) Loss of capacity, not competence, as the fundamental process governing deposition from turbidity currents. *J. Sed. Res*, **64**, 203–214.

Hughes Clarke, J. E., **Marques, C. R. V.** and **Pratomo, D.** (2014) Imaging active mass-wasting and sediment flows on a Fjord Delta, Squamish, British Columbia. In: *Submarine Mass Movements and Their Consequences*(Ed. S. Krastel), pp. 249–260. Springer International Publishing, Cham.

Jobe, Z. R., **Lowe, D. R.** and **Uchytil, S. J.** (2011) Two fundamentally different types of submarine canyons along the continental margin of Equatorial Guinea. *Mar. Petrol. Geol*, **28**, 843–860.

Jorritsma, J. (1973) Sluiting tijdelijke toegang Europoort - onderzoek naar de taludhellingen onder water aangebracht zand - verslag model onderzoek: Waterloopkundig Laboratorium.

Kennedy, J. F. (1960) *Stationary Waves and Antidunes in Alluvial Channels*. California Institute of Technology. Pasadena, CA, 172 pp.

Kennedy, J. F. (1969) The Formation of Sediment Ripples, Dunes, and Antidunes. *Annu. Rev. Fluid Mech.*, **1**, 147–168.

Kidanemariam, A. G. and **Uhlmann, M.** (2014) Direct numerical simulation of pattern formation in subaqueous sediment. *J. Fluid Mech.*, **750**, R2.

Kostic, S. (2011) Modeling of submarine cyclic steps: controls on their formation, migration, and architecture. *Geosphere*, **7**, 294–304.

Kostic, S. (2014) Upper flow regime bedforms on levees and continental slopes: turbidity current flow dynamics in response to fine-grained sediment waves. *Geosphere*, **10**, 1094–1103.

Kostic, S. and **Parker, G.** (2006) The response of turbidity currents to a canyon–fan transition: internal hydraulic jumps and depositional signatures. *J. Hydraul. Res.*, **44**, 631–653.

Kostic, S., **Sequeiros, O.**, **Spinewine, B.** and **Parker, G.** (2010) Cyclic steps: a phenomenon of supercritical

shallow flow from the high mountains to the bottom of the ocean. *J. Hydro-environ. Res.*, **3**, 167–172.

Lamb, M. P., **Parsons, J. D.**, **Mullenbach, B. L.**, **Finlayson, D. P.**, **Orange, D. L.** and **Nittrouer, C. A.** (2008) Evidence for superelevation, channel incision, and formation of cyclic steps by turbidity currents in Eel Canyon, California. *Geol. Soc. Am. Bull.*, **120**, 463–475.

Lang, J. and **Winsemann, J.** (2013) Lateral and vertical facies relationships of bedforms deposited by aggrading supercritical flows: from cyclic steps to humpback dunes. *Sed. Geol.*, **296**, 36–54.

Macdonald, R. G., **Alexander, J.**, **Bacon, J. C.** and **Cooker, M. J.** (2013) Variations in the architecture of hydraulic-jump bar complexes on non-eroding beds.. (S. Dey, Ed.) *Sedimentology*, **60**, 1291–1312.

Maier, K. L., **Fildani, A.**, **Paull, C. K.**, **McHargue, T. R.**, **Graham, S. A.** and **Caress, D. W.** (2013) Deep-sea channel evolution and stratigraphic architecture from inception to abandonment from high-resolution Autonomous Underwater Vehicle surveys offshore central California. *Sedimentology*, **60**, 935–960.

Mastbergen, D. R. and **Van Den Berg, J. H.** (2003) Breaching in fine sands and the generation of sustained turbidity currents in submarine canyons. *Sedimentology*, **50**, 625–637.

Meyer-Peter, E. and **Müller, R.** (1948) Formulas for bed-load transport, in international association for hydraulic structures research, p. 38–64.

Middleton, G. V. (1965) Antidune cross-bedding in a large flume. *J. Sed. Petrol*, **35**, 922–927.

Migeon, S., **Savoye, B.** and **Faugeres, J.-C.** (2000) Quaternary development of migrating sediment waves in the Var deep-sea fan: distribution, growth pattern, and implication for levee evolution. *Sed. Geol.*, **133**, 265–293.

Migeon, S., **Savoye, B.**, **Zanella, E.**, **Mulder, T.**, **Faugeres, J. C.** and **Weber, O.** (2001) Detailed seismic-reflection and sedimentary study of turbidite sediment waves on the var sedimentary ridge (SE France): significance for sediment transport and deposition and for the mechanisms of sediment-wave construction. *Mar. Petrol. Geol.*, **18**, 179–208.

Migeon, S., **Mulder, T.**, **Savoye, B.** and **Sage, F.** (2006) The Var turbidite system (Ligurian Sea, northwestern Mediterranean) —morphology, sediment supply, construction of turbidite levee and sediment waves: implications for hydrocarbon reservoirs. *Geo-Mar. Lett.*, **26**, 361–371.

Nordin, C. F. and **Beverage, J. P.** (1965) *Sediment Transport in the Rio Grande New Mexico*. US Government Printing Office, Washington, DC, 1–35 pp.

Normandeau, A., **Lajeunesse, P.**, **G Poiré, A.** and **Francus, P.** (2016) Morphological expression of bedforms formed by supercritical sediment density flows in four fjord-lake deltas of the south-eastern Canadian Shield (Eastern Canada). *Sedimentology*, **63**, 2106–2129.

Normark, W. R., **Piper, D. J. W.**, **Posamentier, H.**, **Pirmez, C.** and **Migeon, S.** (2002) Variability in form and growth of sediment waves on turbidite channel levees. *Mar. Geol.*, **192**, 23–58.

Parker, G. (1996) Some speculations on the relation between channel morphology and channel-scale flow structures. In: *Coherent Flow Structures in Open Channels* (Eds. P.J. Ashworth, S.J. Bennett, J.L. Best and S.J. McLelland), pp. 424–458. John Wiley and Sons Ltd., London.

Parker, G. and **Izumi, N.** (2000) Purely erosional cyclic and solitary steps created by flow over a cohesive bed. *J. Fluid Mech.*, **419**, 203–238.

Paull, C. K., **Ussler III, W.**, **Caress, D. W.**, **Lundsten, E.**, **Covault, J. a.**, **Maier, K. L.**, **Xu, J.** and **Augenstein, S.** (2010) Origins of large crescent-shaped bedforms within the axial channel of Monterey Canyon, offshore California. *Geosphere*, **6**, 755–774.

Ponce, J. J. and **Carmona, N.** (2011) Coarse-grained sediment waves in hyperpycnal clinoform systems, Miocene of the Austral foreland basin, Argentina. *Geology*, **39**, 763–766.

Postma, G. and **Cartigny, M. J. B.** (2014) Super- and subcritical turbidity currents and their deposits – a synthesis. *Geology*, **16**, 3830.

Postma, G., **Cartigny, M.** and **Kleverlaan, K.** (2009) Structureless, coarse-tail graded Bouma Ta formed by internal hydraulic jump of the turbidity current? *Sed. Geol.*, **219**, 1–6.

Postma, G., **Kleverlaan, K.** and **Cartigny, M. J. B.** (2014) Recognition of cyclic steps in sandy and gravelly turbidite sequences, and consequences for the Bouma facies model. *Sedimentology*, **61**, 2268–2290.

Rouse, H. (1936) Discharge characteristics of the free overfall: use of crest section as a control provides easy means of measuring discharge. *Civ. Eng.*, **6**, 257–260.

Sequeiros, O. E., **Spinewine, B.**, **Garcia, M. H.**, **Beaubouef, R. T.**, **Sun, T.**, **Savoye, B.** and **Parker, G.** (2009) Experiments on wedge-shaped deep sea sedimentary deposits in Minibasins and/or on channel levees emplaced by turbidity currents. Part I. Documentation of the flow. *J. Sed. Res*, **79**, 593–607.

Slootman, A., **Cartigny, M. J. B.**, **Moscariello, A.**, **Chiaradia, M.** and **de Boer, P. L.** (2016) Quantification of tsunami-induced flows on a Mediterranean carbonate ramp reveals catastrophic evolution. *Earth Planet. Sci. Lett.*, **444**, 192–204.

Soldati, A. and **Marchioli, C.** (2012) Sediment transport in steady turbulent boundary layers: potentials, limitations, and perspectives for Lagrangian tracking in DNS and LES. *Adv. Water Resour.*, **48**, 18–30.

Soulsby, R.. (1997). *Dynamics of Marine Sands: A Manual for Practical Applications*. Thomas Telford, London, 253 pp.

Spinewine, B., **Sequeiros, O. E.**, **Garcia, M. H.**, **Beaubouef, R. T.**, **Sun, T.**, **Savoye, B.** and **Parker, G.** (2009) Experiments on wedge-shaped deep sea sedimentary deposits in minibasins and/or on channel levees emplaced by turbidty currents. Part II. *J. Sed. Res*, **79**, 608–628.

Sun, T. and **Parker, G.** (2005) Transportational cyclic steps created by flow over an erodible bed. Part 2. Theory and numerical simulation. *J. Hydraul. Res.*, **43**, 502–514.

Symons, W. O., **Sumner, E. J.**, **Talling, P. J.**, **Cartigny, M. J. B.** and **Clare, M. A.** (2016) Large-scale sediment waves and scours on the modern seafloor and their implications for the prevalence of supercritical flows. *Mar. Geol.*, **371**, 130–148.

Taki, K. and **Parker, G.** (2005) Transportational cyclic steps created by flow over an erodible. *J. Hydraul. Res.*, **43**, 488–501.

Tubau, X., **Paull, C. K.**, **Lastras, G.**, **Caress, D. W.**, **Canals, M.**, **Lundsten, E.**, **Anderson, K.**, **Gwiazda, R.** and **Amblas, D.** (2015) Submarine canyons of Santa Monica Bay, Southern California : variability in morphology and sedimentary processes. *Mar. Geol.*, **365**, 61–79.

Van den Berg, J. H. and **Van Gelder, A.** (1993) *A New Bedform Stability Diagram, With Emphasis on the Transition of Ripples to Plane Bed in Flows Over Fine Sand and Silt* (Eds

M. Marzo and P. C) *Special Publication of the International Association of Sedimentologists* **17**, 11–21.

Van Rijn, L. C. (1984) Sediment transport Part I Bed load transport. *J. Eng. Mech*, **110**, 1431–1456.

Ventra, D., **Cartigny, M. J. B.**, **Bijkerk, J. F.** and **Acikalin, S.** (2015) Supercritical-flow structures on a Late Carboniferous delta front: sedimentologic and paleoclimatic significance. *Geology*, **43**, G36708. 1

Winterwerp, J. C., **de Groot, M. B.**, **Masebrgens, D. R.** and **Verwoert, H.** (1992) Hyperconcentrated sand-water mixutre flows over erodible bed. *J. Hydraul. Eng.*, **118**, 1508–1525.

Wong, M. and **Parker, G.** (2006) Reanalysis and Correction of Bed-Load Relation of Meyer-Peter and Müller Using Their Own Database. *J. Hydraul. Eng.*, **132**, 1159–1168.

Wynn, R. B. and **Stow, D. A. V.** (2002) Classification and characterisation of deep-water sediment waves. *Mar. Geol.*, **192**, 7–22.

Yagishita, K. and **Taira, A.** (1989) Grain fabric of a laboratory antidune. *Sedimentology*, **36**, 1001–1005.

Yokokawa, M., **Okuno, K.**, **Nakamura, A.**, **Muto, T.**, **Miyata, Y.** and **Naruse, H.** (2009) Aggradational cyclic steps: sedimentary structures found in flume experiments.: Proceedings 33rd IAHR Congress. *Vancouver*, **81**, 5547–5554.

Zhong, G., **Cartigny, M. J. B.**, **Kuang, Z.** and **Wang, L.** (2015) Cyclic steps along the South Taiwan Shoal and West Penghu submarine canyons on the northeastern continental slope of the South China Sea. *Geol. Soc. Am. Bull.*, **127**, 804–824.

APPENDIX

Governing equations Reynolds-Averaging Navier-Stokes (RANS) and turbulence models

Mass balance equation:

$$\frac{\partial \rho}{\partial t}+\frac{\partial}{dx}(\rho u)+\frac{\partial}{dy}(\rho v)+\frac{\partial}{dz}(\rho w)=0 \qquad (1.1)$$

Momentum Balance equations:

$$\frac{\partial u}{\partial t}+u\frac{\partial u}{\partial x}+v\frac{\partial u}{\partial y}+w\frac{\partial u}{\partial x}=-\frac{1}{\rho}\frac{\partial p}{\partial x}+G_x+f_x \quad (1.2)$$

$$\frac{\partial v}{\partial t}+u\frac{\partial v}{\partial x}+v\frac{\partial v}{\partial y}+w\frac{\partial v}{\partial x}=-\frac{1}{\rho}\frac{\partial p}{\partial y}+G_y+f_y \quad (1.3)$$

$$\frac{\partial w}{\partial t}+u\frac{\partial w}{\partial x}+v\frac{\partial w}{\partial y}+w\frac{\partial w}{\partial x}=-\frac{1}{\rho}\frac{\partial p}{\partial z}+G_z+f_z \qquad (1.3)$$

Turbulent kinetic energy balance:

$$\frac{\partial k_T}{\partial t}+\left(u\frac{\partial k_T}{\partial x}+v\,\frac{\partial k_T}{\partial y}+w\,\frac{\partial k_T}{\partial z}\right)=\;P_T+D_K-\varepsilon_T \qquad (1.5)$$

Turbulent dissipation balance:

$$\frac{\partial \varepsilon_T}{\partial t}+\left(u\frac{\partial \varepsilon_T}{\partial x}+v\,\frac{\partial \varepsilon_T}{\partial y}+w\,\frac{\partial \varepsilon_T}{\partial z}\right)=\;\frac{C_{\varepsilon 1}\,\varepsilon_T}{k_T}P_T+D_\varepsilon-C_{\varepsilon 2}\frac{\varepsilon_T^2}{k_T} \qquad (1.6)$$

From turbulence to dynamic viscosity:

$$v_T=0\cdot 085\frac{k_T^2}{\varepsilon_T} \qquad (1.7)$$

$$\mu=\rho(v_m+v_t) \qquad (1.8)$$

Further details on the k-epsilon RNG turbulence model can be found in (Basani *et al.*, 2014).

Equations governing sediment transport model

Shields numbers:

$$\theta=\frac{\tau}{gd\left(\rho_s-\rho_f\right)} \qquad (2.1)$$

$$\theta_{cr}=\frac{0\cdot 3}{1+1\cdot 2d_*}+0.55\left(1-e^{-0\cdot 02d*}\right) \qquad (2.2)$$

$$d_*=d\left(\frac{g(\rho_s/\rho_f-1)}{v_f}\right)^{1/3} \qquad (2.3)$$

$$\theta'_{cr}=\theta_{cr}\frac{\cos(\psi)\sin(\chi)+\sqrt{\cos^2(\chi)\tan^2(\omega)-\sin^2(\psi)\sin^2(\chi)}}{\tan(\varphi)} \qquad (2.4)$$

Bed-load transport:

$$q_b=f_s\beta(\theta_i-\theta_{cr})^{1\cdot 5}\left[g\left(\frac{\rho_s-\rho_f}{\rho_f}\right)d_s^3\right]^{\frac{1}{2}} \qquad (2.5)$$

$$\delta=d\left[0\cdot 3d_*^{0\cdot 7}(\theta/\theta_{cr}-1)^{0\cdot 5}\right] \qquad (2.6)$$

$$\mathbf{u_{bedload}} = \frac{q_b}{\delta}\frac{\bar{u}}{||\bar{u}||} \tag{2.7}$$

Suspended-load transport:

$$\mathbf{u_{lift}} = \alpha_i n_s d_*^{0{\cdot}3}(\theta_i - \theta_{cr})^{1{\cdot}5}\sqrt{\frac{||g||d\left(\rho_s - \rho_f\right)}{\rho_f}} \tag{2.8}$$

$$\mathbf{u_{settle}} = \frac{g}{g}\left[\left(10 \cdot 36^2 + 1 \cdot 049 d_*^3\right)^{1/2} - 10 \cdot 36\right]\frac{\nu_f}{d} \tag{2.9}$$

$$\mathbf{u_s} = \bar{\mathbf{u}} + \mathbf{u_{settle}} C_{\mathrm{vol}} \tag{2.10}$$

$$\frac{\partial c}{\partial_t} + \nabla \cdot (\mathbf{u_s C}_{\mathrm{mass}}) = \nabla \cdot \nabla(\mathbf{D C}_{\mathrm{mass}}) \tag{2.11}$$

$$D = \frac{RMSC \cdot \mu}{\rho_f} + \frac{CMSC}{\rho_f} \tag{2.12}$$

$$c_{\mathrm{vol}} = \frac{C_{\mathrm{mass}}}{\rho_s} \tag{2.13}$$

List of symbols

$A_{x,y,z}$	Fractional area
C_{mass}	Suspended sediment mass-concentration
C_{vol}	Suspended sediment volume concentration
CMSC	Coefficient of diffusion
$C_{\varepsilon 1,\varepsilon 2}$	Dimensionless parameter
D	Diffusion coefficient
D_K	Turbulent kinetic energy diffusion term
D_ε	Diffusion of dissipation of turbulence term
d	Grain size
d_*	Dimensionless grain parameter
$f_{x,y,z}$	Viscous accelerations
Fr	Froude number
g	Gravitational acceleration
$G_{x,y,z}$	Body accelerations
k_T	Turbulent kinetic energy
P_T	Turbulent kinetic energy production term
q_b	Bed-load transport rate
RMSC	Inverse Schmidt number
$\mathbf{u_s}$	Velocity of the suspended sediment
$\bar{\mathbf{u}}$	Mean velocity of water-sediment mixture, obtained via Navier-Stokes
$\mathbf{u_{lift}}$	Lift velocity
$\mathbf{u_{bedload}}$	Bed-load velocity
$\mathbf{u_{settle}}$	Sediment settling mass-flux
α	Entrainment coefficient
β	Bed-load coefficient
δ	Thickness bed-load layer
ε_T	Turbulent dissipation
θ	Local Shields number
θ_{cr}	Critical Shields number
μ	Dynamic viscosity
ν_f	Kinematic viscosity of water
ρ_s	Density of the sediment
ρ_f	Density of the fluid
$\bar{\rho}$	Mean density fluid-sediment mixture
τ	Shear stress
τ_{cr}	Critical shear stress
χ	Angle slope of bed
ψ	Angle between flow and upslope direction
ω	Angle of repose

Manuscript received 17 August 2016; revision accepted 19 May 2017

Supporting Information

Additional Supporting Information may be found in the online version of this article:

Video S1. A video of simulation 2. The video shows the behaviour of the cyclic step system. Both in terms of fluid character as well as in sediment bed development.

Video S2. A video of simulation 2. The video shows the internal structure of the cyclic step bedforms with two-second timelines, and the water surface.